Improved multi-site Parkinson's disease classification using neuroimaging data with counterfactual inference

Author name(s) withheld EMAIL(S) WITHHELD
Address withheld

Editors: Under Review for MIDL 2023

Abstract

Deep learning has led to many advances in medical image analysis for various clinical problems. However, most deep learning models are known to be sensitive to differences in the training and test data distributions, which can lead to a decrease in accuracy when applied in real-life scenarios. Thus far, various techniques have been developed to tackle this problem, primarily focusing on harmonizing feature representations from different datasets. Due to the recent increased interest in causal approaches in deep learning, explainable harmonization techniques have gained momentum lately but have not been applied broadly yet. Our study proposes a causal flow-based technique to overcome the problem of different feature distributions in multi-site data used for Parkinson's disease (PD) classification. Feature distributions from six different sites, with a total of 415 subjects (PD: 263, healthy controls: 152), were used for the experiments. A counterfactual approach to answer the question, "How would brain MRI features appear if they were obtained at a different site?" was developed using a causal normalizing flow. When tested on features from a previously unseen site, the counterfactual-based classifier demonstrated superior performance (weighted f1 = 0.68) compared to a classifier trained on purely observational data (weighted f1 = 0.36) and improved accuracy compared to a harmonization technique typically used in neurological settings (weighted f1 = 0.5). These results show that the proposed technique can effectively correct differences in multi-site feature distributions to facilitate generalizable deep-learning models.

Keywords: Domain shift, harmonization, normalizing flow, causality, counterfactual, Parkinson's disease

1. Introduction

As in many other domains, medical image analysis has benefited tremendously from the recent advancements in deep learning. However, deep learning models are known to be prone to decreased accuracy when applied to datasets with a distribution that differs from datasets used for training (Robinson et al., 2020). This phenomenon, known as domain shift, can be caused by acquisition shifts, population shifts, or a combination thereof. An acquisition shift occurs when there are variations regarding the imaging modalities, procedures, or scanners used, while a population shift can occur when the subject groups have different characteristics, such as demographics or disease states. Both shifts may also occur in multi-center studies making it often difficult to train generalizable machine learning models. Addressing these domain shifts is critical for improving performance across multiple sites, avoiding biases in the results, and developing generalizable deep learning models for health care.

© 2023 Anonymous.

One way to overcome the problems of domain shifts is to collect and train the models with large datasets. However, this approach has several limitations. First, collecting diverse and unbiased data can be time-consuming and labeling the data can be laborious. Additionally, training a single model to perform well across multiple sites with varying domain shifts may result in a trade-off between accuracy and generalization. Thus, it may be necessary to re-train deep learning models with new data to ensure that they perform well using data from new sites. As an alternative, researchers have explored the use of domain adaptation techniques to overcome these problems (Farahani et al., 2020), which aim to learn domain-invariant feature representations.

Domain adaptation in machine learning often involves, but is not limited to, disentangling domain-specific features from datasets or enforcing a specific distribution on the latent representations of the inputs. Typically, ComBat (Johnson et al., 2007) and its variants are used for this purpose. This empirical Bayes method aims to remove effects specific to a particular scanner or site while maintaining the relevant features of the data. A potential drawback of this approach is that it may also remove unknown confounders during the site adaptation process, decreasing the model's overall accuracy. More recently, deep generative networks, including generative adversarial networks (GANs) and variational autoencoders (VAEs), have been used for this purpose due to their ability to reconstruct images from different domains (Zhu et al., 2017; Mathieu et al., 2019). However, a major limitation of these generative approaches is their lack of interpretability and explainability, as they operate mostly as black boxes (Vasudevan et al., 2021).

Recently, causal approaches have started gaining popularity in the deep learning community to overcome the problems associated with black box machine learning models. The explicit modeling of causal relationships in deep learning settings makes the models more explainable. At the same time, it can address the issues of learning spurious correlation during training and being sensitive to domain-specific statistics. For this reason, recent studies have also started integrating causality for disentanglement tasks (Goudet et al., 2018; Bengio et al., 2019; Parascandolo et al., 2018; Yang et al., 2021). In the context of our study, causal analysis can be used to remove the effects of a particular site/scanner from the feature distributions using counterfactuals. The counterfactual inference is essentially asking the query from the trained causal model, "How would the features look like if they had been acquired at a different site?". This query synthesizes a new set of features with similar distribution characteristics from the specified site, thereby minimizing domain shifts. Thus far, such queries have been limited to a few variables, and to accurately perform them on high-dimensional data, deep invertible models that explicitly map densities are required.

Normalizing flows (NF) are a class of deep generative models that explicitly model complex data distributions (Kobyzev et al., 2021). This is achieved by representing the density of the data as an invertible transformation of a noise variable with a simple distribution using the change of variable formula. Pawlowski et al. (2020) have developed a deep structural causal model combining causality, NF, and VAEs. This causal model was able to generate realistic counterfactual images using the Morpho-MNIST and brain MRI datasets. In a subsequent study, Wang et al. (2021) applied this framework for harmonizing multi-site image features. However, this framework requires separate conditional density estimation (Trippe and Turner, 2018) to encode the causal structure in the data. As an alternative approach, Wehenkel and Louppe (2020) argued that NF on itself could be understood as a

causal model if the order of conditioners (autoregressive or coupling) was defined correctly. Following this, Khemakhem et al. (2021) proved that causal structural equation models (SEM) could be modeled using standard NFs and developed the causal autoregressive flow (CAREFL) framework. They generated counterfactual queries using a synthetic dataset of two cause and two effect variables and validated them.

This study builds upon the CAREFL framework to create counterfactual features from multi-site brain MRI data. Specifically, the main contributions of this work are (1) extending the CAREFL framework's coupling conditioner to work with different sizes of cause and effect variables and (2) for the first time, using a causal NF without external conditioning for data harmonization. Results from this study show that causal flow-based techniques could effectively correct differences in feature distributions, leading to generalizable deep learning models.

2. Background

2.1. Structural equation modeling

Structural equation modeling (SEM) is a well-known method for analyzing relationships between variables, both observed and latent, by creating a model that represents the relationships as equations. Let's assume that the feature vector $\mathbf{x}$ is d-dimensional and consists of features $\mathbf{x} = (x_1, x_2, ..., x_d)$ with a joint probability distribution P_{x}. The structural equation for each variable x_j is defined as $S_j : x_j = f_j(pa_j, n_j)$, where pa_j denotes the parent of x_j in the causal model and n_j represents the mutually independent exogenous noise variable of the noise distribution P_{n}. Then, a SEM is defined as (S, P_{n}), where $S = \{S_1, S_2, ..., S_j\}$. In this formulation, the observational distribution of variables (P_{x}) can be thought of as being generated by sampling from a noise distribution (P_n) and then applying a set of structural equations (S) to the sampled values. This means that the observed variables are influenced by the noise distribution as well as the relationships represented by the structural equations. A directed acyclic graph (DAG), $\mathcal{G}$, either discovered or provided, is typically used to define the causal relationship between the variables. In $\mathcal{G}$, each node corresponds to a variable x_j, and the directed edges denote the causal ordering of the variables. In this context, structural equations can be rewritten as

$$x_j = f_j(x < \pi(j), n_j) \tag{1}$$

where $x < \pi(j)$ represents all variables before x_j in the causal ordering defined by the graph.

2.2. SEM with Normalizing flows

Normalizing flows model a complex probability distribution p_{x} as the result of a series of transformations $\mathbf{T}$ applied to a predefined probability density p_{z}, typically chosen as Gaussian (Kobyzev et al., 2021). $\mathbf{T}$ has to be invertible and differentiable to train the model using the change of variables formula

$$P_{\mathrm{x}}(\mathbf{x}) = P_{\mathrm{z}}(\mathbf{T}^{-1}(\mathbf{x}))|\det\ J_{\mathbf{T}^{-1}}(\mathbf{x})| \tag{2}$$

where $\det\ J_{\mathbf{T}^{-1}}$ is the determinant of Jacobian $J_{\mathbf{T}^{-1}}$. The series of transformations $T = T_1 \circ \cdots \circ T_k$ is typically implemented using neural networks while conditioning the Jacobian as a

lower triangular matrix for efficient computation of the determinant. Coupling conditioners are typically used in normalizing flows to yield a lower triangular J. The conditioners c_j for each variable x_j are defined as:

$$c_j = \begin{cases} \underline{h}_j & \text{if } j \leq k \\ h_j([x_1 \cdots x_k]) & \text{if } j > k \end{cases} \tag{3}$$

where $\underline{h}_j$ denotes constant values and h_j is a function of previous x values, and $k \in [1, d]$ is a hyperparamter. Thus, each transformed input variable from the corresponding latent variable z_j is given by:

$$x_j = T_j(z_j, c_j) \tag{4}$$

One might notice the similarity between the equations 1 and 4. More precisely, both models define a specific order for variables and assume that the latent variables z_j follow simple distributions. This ordering can be determined from a causal DAG using D-separation, which reveals conditional independence in the graph. The conditioning c_j for each variable x_j in normalizing flows can be set based on this identified conditional independence, and this ordering of the conditioning must be maintained throughout the flow. For more information on this topic, the reader can refer to the works of Wehenkel and Louppe (2021) and Khemakhem et al. (2021).

2.3. Counterfactual inference

Counterfactual queries aim to assess statements about hypothetical situations. For example, if variable x_j had taken the value $x_j = \alpha$ in our observed feature vector $\mathbf{x}^{obs}$, what would be the value of variable x_i? This is denoted as $x_{i,x_j \leftarrow \alpha}$. According to Pearl (2009), evaluating causal counterfactuals requires three steps: abduction, action, and prediction. After fitting an NF to the data, abduction evaluates the posterior distribution over latent variables $\mathbf{z}^{obs}$ given observations $\mathbf{x}^{obs}$. In normalizing flow models, this can be simply done by computing the transformation $\mathbf{z}^{obs} = \mathbf{T}^{-1}(\mathbf{x}^{obs})$ to identify the corresponding latent values, where $\mathbf{z}^{obs}$ is the latent representation. The next step is to intervene and fix the value of x_j to a specific value α, which makes it independent of its causes pa_j and noise n_j. This is referred to as the action step and is denoted by $do(x_j = \alpha)$. In this step, the corresponding value of change of $x_{i,x_j \leftarrow \alpha}$ is adjusted in the latent space $\mathbf{z}_j^{obs}$. After intervening, the new feature vector $\mathbf{x}^{cf}$ is predicted by computing a transformation pass of the intervened $\mathbf{z}^{obs}$ in the NF model.

3. Material and Methods

3.1. Data

We utilized data from 6 sites, including 415 subjects (263 with Parkinson's disease and 152 healthy) to develop and evaluate our methods. The studies included were the BioCog (Clinical, Magnetic Resonance, and Genetic Biomarkers of Cognitive Decline and Dementia in Parkinson's Disease) (Acharya et al., 2007), C-BIG (Montreal Neurological Institute's Open Science Clinical Biological Imaging and Genetic Repository), Neurocon (Badea et al., 2017), Tao Wu (Badea et al., 2017), OpenNeuro Japan(Noritaka et al., 2018), and PD MCI

Calgary (Lang et al., 2019). For this work, we included subjects with T1-weighted magnetic resonance imaging (MRI) datasets with known ground truth labels (PD or healthy controls). All studies included in this work received ethics approval from their local ethics boards and written informed consent from all the participants in accordance with the Declaration of Helsinki.

In the initial step, the T1-weighted images were pre-processed to remove non-brain tissue using HD-BET (Isensee et al., 2019), resampled to 1mm isotropic resolution employing a linear interpolation, and corrected for bias field distortions (Tustison et al., 2010). Afterwards, each T1-weighted MRI dataset was registered non-linearly to the MNI PD25 atlas. The Harvard-Oxford (HO) cortical and subcortical segmentations available in the atlas space were then transformed inversely using nearest-neighbor interpolation for each subject. The HO atlas contained volumes of 69 brain regions, including the hippocampus, caudate, and insular cortex, which were calculated from the transformed atlas and normalized based on the intracranial volume. The final dataset comprised 70 features, including the intracranial volume. Figure 1(left) displays the distribution of the normalized right hippocampus volume for each site. It can be observed that there are inter-site variations in the distribution, which could potentially be attributed to population and acquisition shifts.

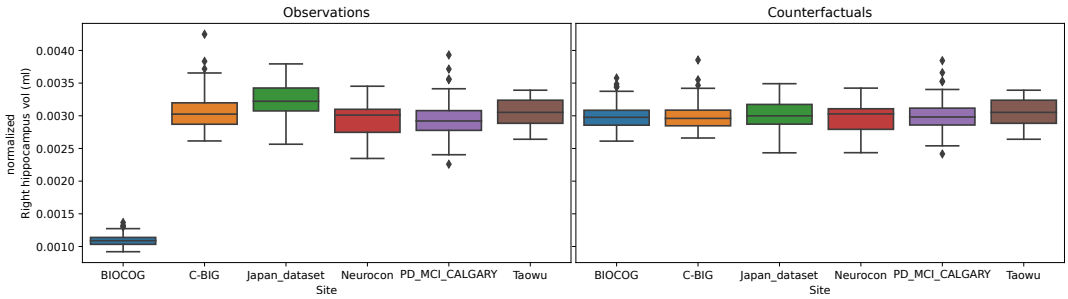

Figure 1: The figure shows the multi-site distribution of the observed right hippocampus volume on the left and the inferred counterfactual distribution of the same features on the right (base site for counterfactual: PD MCI Calgary).

3.2. Counterfactual inference of sites

In the first step, a causal DAG was defined with the assumption that the site variable influences every feature and that there is no interaction between features. Then, we asked the counterfactual query, "How would the features look if they had been acquired at a different site?". By following the abduction, action, and prediction steps mentioned in section 2.3, counterfactual features were generated with respect to the base site. Specifically, the site variable s_i was set to the base site b as $do(s_i = b)$. Then, the flow was computed to generate the counterfactual features.

A coupling conditioner was designed to encode this DAG into the normalizing flow architecture (see equation 3), and the order of the coupling was maintained throughout the layers. The normalizing flow model consisted of 10 transformation layers similar to realnvp

(real-valued non-volume preserving) layers (Dinh et al., 2017). A multi-layer perceptron with three hidden layers, each layer having ten neurons, was used to determine the transformation parameters. As usual for a bijective flow model, the layer's size was the input feature size, which was consistent for every layer. All input features were normalized during training using the mean and the standard deviation. For learning, the Adam optimizer was used with a learning rate of 0.0005 and a batch size of 128. A negative log-likelihood estimator determined the loss of the training, where the standard normal distribution was used as the latent distribution.

3.3. Classification network

In order to evaluate the benefit of using the proposed data harmonization technique, a simple PD classification model was developed and trained using the raw as well as corrected volume features. A multi-layer perceptron with three hidden layers was used for this purpose. The input layer size was 70, equal to the number of brain MRI features extracted. The subsequent hidden layers had 64, 32, and 16 neurons, batch normalization, and ReLU activations. The output layer employed sigmoid activation, and binary cross-entropy was used as the loss function. Since the number of PD versus healthy subjects was not balanced, we used a weighted random sampler with replacement for the batching. For optimization, Adam was used with the following parameters: learning rate = 0.005, weight decay = 0.0001, and batch size = 64. During training, the validation accuracy was tracked, and the model with the best validation accuracy was chosen, whereas twenty percent of the training data was used for the validation. PyTorch was used for the implementation, and the model was trained using a 32GB NVIDIA 3090 graphics card.

3.4. Experimental setup

Following the feature extraction, the final dataset consisted of the study name ($\mathbf{s}$), 70 brain MRI features (X), and a label for disease classification ($\mathbf{y}$). Next, the datasets were split as 60% for the training and 40% for the testing. The ratio of PD vs healthy in the dataset was maintained as the same in training and testing datasets through stratification. For the experiments, studies were divided into three sets: base site (B), existing sites (E), and new site (N). The new site N was selected to be the site with drastically different characteristics and used to simulate the scenario in that the model is used to classify unseen data. More precisely, N was chosen to be BioCog, and one site from {Neurocon, Japan, PD MCI Calgary, C-BIG, Tao Wu} was selected as B and the rest as E.

In the first step, a normalizing flow model was trained separately for each site, with site B as the base. For each site e, features X_e^{train} and X_B^{train} were used for this purpose. After training, counterfactual data was generated for both train and test data from each site e and denoted as $X_{e\leftarrow B}^{\text{train}}$ and $X_{e\leftarrow B}^{\text{test}}$. These steps are schematically shown in Fig. 2, and the inferred counterfactual features for each site are shown in Fig. 1(right). It is important to note that $\mathbf{y}$ was not used in the NF models to simulate unlabeled data and to avoid labels leaking into the flow models during testing.

To evaluate the benefit of the proposed data harmonization method, we trained three classifiers, C_{obs}, C_{ComBat}, and C_{cf} with the same hyper-parameters, one with true observational data, one with ComBat harmonization, and the other with counterfactuals. ComBat

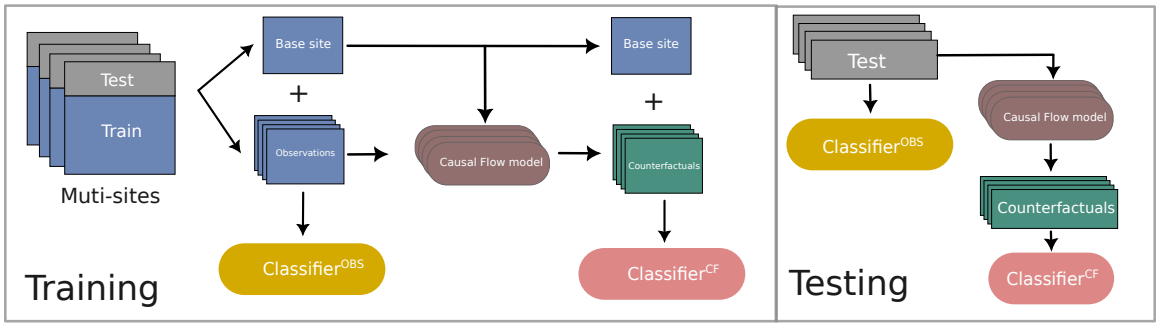

Figure 2: The training and testing process of the proposed framework. Training dataset was used to train flow and classifier models, and F1-score was calculated on the test dataset.

(Johnson et al., 2007) is a data harmonization technique typically used in neurological settings to harmonize multisite image-derived features. The open-sourced python code from the authors was used for the implementation of ComBat harmonization (Fortin et al., 2018).

As the next step, $D_{\text{obs}}^{\text{train}}$ $(X_{E+B}^{\text{train}}, \mathbf{y}_{E+B}^{\text{train}})$ was used for the training of C_{obs} and ComBat harmonized data $D_{\text{ComBat}}^{\text{train}}$ for C_{ComBat}. Similarly for C_{cf}, training dataset $D_{\text{cf}}^{\text{train}}$ ($X_{(E\leftarrow B)+B}^{\text{train}}, \mathbf{y}_{E+B}^{\text{train}}$) was used. Final testing was done using $D_{\text{obs}}^{\text{test}}$, $D_{\text{ComBat}}^{\text{test}}$ and $D_{\text{cf}}^{\text{test}}$ on C_{obs}, C_{ComBat}, and C_{cf}, respectively. Next, it was tested how the model behaved when it was presented with unseen data. Using the trained models C_{obs}, C_{ComBat} and C_{cf}, test data from the new site, respective ComBat harmonized data, and counterfactual data were tested respectively.

4. Results

First, the accuracy of the NF models was validated by comparing the predicted and observational distributions (Appendix A). Then, PD classification accuracy was measured on test datasets using both predicted and observational features. For this, separate classifiers were trained with these 70 features as inputs. The test results of C_{obs}, C_{ComBat}, and C_{cf} (base: C-BIG) are shown in Fig. 3, which displays the improvement in the overall test accuracy after making the counterfactual inference. Specifically, the PD MCI CALGARY site showed significant improvement in accuracy compared to observational and ComBat harmonized data.

When unseen data was tested with the classifiers, the counterfactual-based classifier showed substantially better performance (weighted f1 = 0.68) compared to a classifier trained on purely observational data (weighted f1 = 0.36) and ComBat-harmonized data (weighted f1 = 0.50). It can be noted that before counterfactual inference, all observational data from the unseen site was classified as healthy because of the difference in the distributions. The same experiment was conducted with different base sites, and their accuracy is presented in Table 3, where precision and recall results are presented in Appendix B.

Similar test accuracies were observed for classifiers with different base sites, showing that the choice of the base site does not affect the classification.

Table 1: Weighted F1-scores of classifiers trained with different base sites. CF: Causal flow based technique, PMC: PD MCI CALGARY

Base site	Technique	C-BIG	Japan	Neurocon	Taowu	PMC	BIOCOG
-	-	0.67	0.56	0.48	0.66	0.59	0.36
C-BIG	CF	0.65	0.62	0.5	0.6	0.64	0.68
	ComBat	0.66	0.6	0.48	0.63	0.46	0.5
Japan	CF	0.65	0.62	0.5	0.6	0.64	0.74
	ComBat	0.66	0.6	0.48	0.63	0.46	0.5
Neurocon	CF	0.67	0.62	0.5	0.53	0.66	0.7
	ComBat	0.66	0.6	0.48	0.63	0.46	0.5
Taowu	CF	0.67	0.62	0.5	0.6	0.64	0.71
	ComBat	0.66	0.6	0.48	0.63	0.46	0.5
PMC	CF	0.67	0.62	0.5	0.6	0.61	0.68
	ComBat	0.66	0.6	0.48	0.63	0.46	0.5

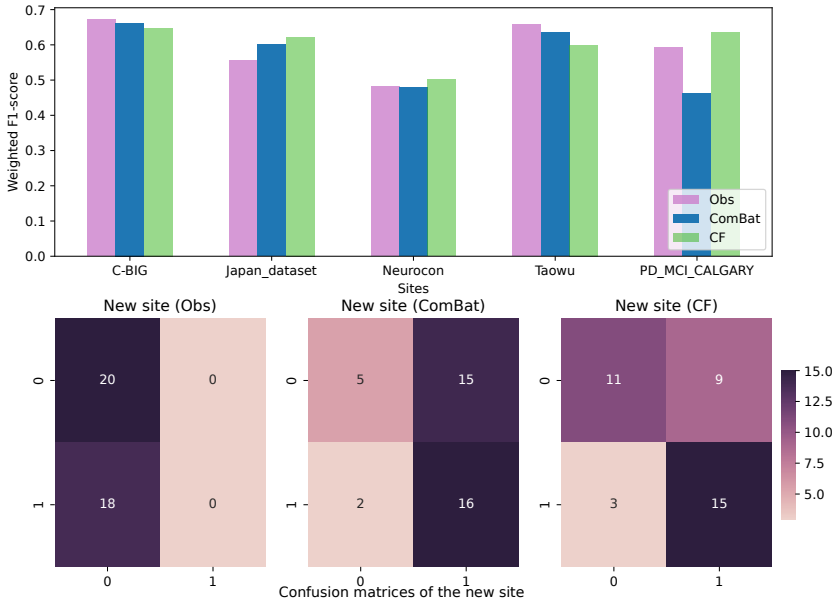

Figure 3: Top: PD classification accuracy of true observed data (Obs), ComBat harmonized data (ComBat), and counterfactuals (CF) using C-BIG as the base site. Bottom: test results for an unseen site represented by the confusion matrix.

Furthermore, we analyzed which features are predominantly affected by the proposed harmonization technique. The mean squared error (MSE) was calculated by comparing the observational and counterfactual data from the BIOCOG site. The five most affected features and their respective MSE values are as follows: left cerebral cortex=0.0279, right cerebral cortex = 0.0276, right cerebral white matter=0.0067, left cerebral white matter=0.0066, frontal pole=0.0014.

5. Conclusion

This study investigates causal counterfactual inference as an approach to data harmonization to address differences in feature distributions in multi-site data used for Parkinson's disease (PD) classification. Unlike other generative techniques, the causal normalizing flow method explicitly models the relationships between variables based on a causal structure with a tractable density, enabling direct counterfactual inference. Furthermore, in contrast to other flow-based harmonization methods, this proposed technique facilitates the construction of causal graphs without external conditioning. Using this approach, we sought to answer the question, "How would brain MRI features appear if they were obtained from a different site?". The inferred counterfactual-based classifier's overall accuracy was better than that of a classifier trained on purely observational data. When tested on features from a previously unseen site, the counterfactual-based classifier demonstrated improved performance compared to ComBat, a technique typically used in neurological settings. These results indicate that the proposed technique can effectively harmonize the multi-site distributions to facilitate generalizable deep learning models. Furthermore, this technique can easily be extended to images as well as other relevant areas, such as fairness and bias mitigation in deep learning.

Acknowledgments

Acknowledgments withheld.

References

Hernish J. Acharya, Thomas P. Bouchard, Derek J. Emery, and Richard M. Camicioli. Axial Signs and Magnetic Resonance Imaging Correlates in Parkinson's Disease. *Canadian Journal of Neurological Sciences*, 34(1):56–61, February 2007. ISSN 0317-1671, 2057-0155. doi: 10.1017/S0317167100005795. URL https://www.cambridge.org/core/journals/canadian-journal-of-neurological-sciences/article/axial-signs-and-magnetic-resonance-imaging-correlates-in-parkinsons-disease/88683D0B3B0F2675A42D18249EAE856D. Publisher: Cambridge University Press.

Liviu Badea, Mihaela Onu, Tao Wu, Adina Roceanu, and Ovidiu Bajenaru. Exploring the reproducibility of functional connectivity alterations in Parkinson's disease. *PLOS ONE*, 12(11):e0188196, November 2017. ISSN 1932-6203. doi: 10.1371/journal.pone.0188196. URL https://journals.plos.org/plosone/article?id=10.1371/journal.pone.0188196. Publisher: Public Library of Science.

Yoshua Bengio, Tristan Deleu, Nasim Rahaman, Rosemary Ke, Sébastien Lachapelle, Olexa Bilaniuk, Anirudh Goyal, and Christopher Pal. A Meta-Transfer Objective for Learning to Disentangle Causal Mechanisms, February 2019. URL http://arxiv.org/abs/1901.10912. arXiv:1901.10912 [cs, stat].

Laurent Dinh, Jascha Sohl-Dickstein, and Samy Bengio. Density estimation using Real NVP, February 2017. URL http://arxiv.org/abs/1605.08803. arXiv:1605.08803 [cs, stat] version: 3.

Abolfazl Farahani, Sahar Voghoei, Khaled Rasheed, and Hamid R. Arabnia. A Brief Review of Domain Adaptation, October 2020. URL http://arxiv.org/abs/2010.03978. arXiv:2010.03978 [cs].

Jean-Philippe Fortin, Nicholas Cullen, Yvette I. Sheline, Warren D. Taylor, Irem Aselcioglu, Philip A. Cook, Phil Adams, Crystal Cooper, Maurizio Fava, Patrick J. McGrath, Melvin McInnis, Mary L. Phillips, Madhukar H. Trivedi, Myrna M. Weissman, and Russell T. Shinohara. Harmonization of cortical thickness measurements across scanners and sites. *NeuroImage*, 167:104–120, February 2018. ISSN 1053-8119. doi: 10.1016/j.neuroimage.2017.11.024. URL https://www.sciencedirect.com/science/article/pii/S105381191730931X.

Olivier Goudet, Diviyan Kalainathan, Philippe Caillou, Isabelle Guyon, David Lopez-Paz, and Michèle Sebag. *Learning Functional Causal Models with Generative Neural Networks*. 2018. doi: 10.1007/978-3-319-98131-4. URL http://arxiv.org/abs/1709.05321. arXiv:1709.05321 [stat].

Fabian Isensee, Marianne Schell, Irada Pflueger, Gianluca Brugnara, David Bonekamp, Ulf Neuberger, Antje Wick, Heinz-Peter Schlemmer, Sabine Heiland, Wolfgang Wick, Martin Bendszus, Klaus H. Maier-Hein, and Philipp Kickingereder. Automated brain extraction of multisequence MRI using artificial neural networks. *Human Brain Mapping*, 40(17):4952–4964, 2019. ISSN 1097-0193. doi: 10.1002/hbm.24750. URL https://onlinelibrary.wiley.com/doi/abs/10.1002/hbm.24750. _eprint: https://onlinelibrary.wiley.com/doi/pdf/10.1002/hbm.24750.

W. Evan Johnson, Cheng Li, and Ariel Rabinovic. Adjusting batch effects in microarray expression data using empirical Bayes methods. *Biostatistics*, 8(1):118–127, January 2007. ISSN 1465-4644. doi: 10.1093/biostatistics/kxj037. URL https://doi.org/10.1093/biostatistics/kxj037.

Ilyes Khemakhem, Ricardo Pio Monti, Robert Leech, and Aapo Hyvärinen. Causal Autoregressive Flows, February 2021. URL http://arxiv.org/abs/2011.02268. arXiv:2011.02268 [cs, stat].

Ivan Kobyzev, Simon J. D. Prince, and Marcus A. Brubaker. Normalizing Flows: An Introduction and Review of Current Methods. *IEEE Transactions on Pattern Analysis and Machine Intelligence*, 43(11):3964–3979, November 2021. ISSN 0162-8828, 2160-9292, 1939-3539. doi: 10.1109/TPAMI.2020.2992934. URL http://arxiv.org/abs/1908.09257. arXiv:1908.09257 [cs, stat].

Stefan Lang, Alexandru Hanganu, Liu Shi Gan, Mekale Kibreab, Noémie Auclair-Ouellet, Tazrina Alrazi, Mehrafarin Ramezani, Jenelle Cheetham, Tracy Hammer, Iris Kathol, Justyna Sarna, and Oury Monchi. Network basis of the dysexecutive and posterior cortical cognitive profiles in Parkinson's disease. *Movement Disorders*, 34(6):893–902, 2019. ISSN 1531-8257. doi: 10.1002/mds.27674. URL https://onlinelibrary.wiley.com/doi/abs/10.1002/mds.27674. _eprint: https://onlinelibrary.wiley.com/doi/pdf/10.1002/mds.27674.

Emile Mathieu, Tom Rainforth, N. Siddharth, and Yee Whye Teh. Disentangling Disentanglement in Variational Autoencoders, June 2019. URL http://arxiv.org/abs/1812.02833. arXiv:1812.02833 [cs, stat].

Yoneyama Noritaka, Watanabe Hirohisa, Kawabata Kazuya, Bagarinao Epifanio, Hara Kazuhiro, Tsuboi Takashi, Tanaka Yasuhiro, Ohdake Reiko, Imai Kazunori, Ogura Rei, Kato Yasutaka, Masuda Michihito, Hattori Tatsuya, Ito Mizuki, Maesawa Satoshi, Mori Daisuke, Katsuno Masahisa, and Sobue Gen. ds000245_r1.0.0, 2018. Dataset.

Giambattista Parascandolo, Niki Kilbertus, Mateo Rojas-Carulla, and Bernhard Schölkopf. Learning Independent Causal Mechanisms, September 2018. URL http://arxiv.org/abs/1712.00961. arXiv:1712.00961 [cs, stat].

Nick Pawlowski, Daniel Coelho de Castro, and Ben Glocker. Deep Structural Causal Models for Tractable Counterfactual Inference. In *Advances in Neural Information Processing Systems*, volume 33, pages 857–869. Curran Associates, Inc., 2020. doi: arXiv:2006.06485. URL https://proceedings.neurips.cc/paper/2020/hash/0987b8b338d6c90bbedd8631bc499221-Abstract.html.

Judea Pearl. *Causality*. Cambridge University Press, Cambridge, 2 edition, 2009. ISBN 978-0-521-89560-6. doi: 10.1017/CBO9780511803161. URL https://www.cambridge.org/core/books/causality/B0046844FAE10CBF274D4ACBDAEB5F5B.

Robert Robinson, Qi Dou, Daniel Coelho de Castro, Konstantinos Kamnitsas, Marius de Groot, Ronald M. Summers, Daniel Rueckert, and Ben Glocker. Image-Level Harmonization of Multi-site Data Using Image-and-Spatial Transformer Networks. In Anne L. Martel, Purang Abolmaesumi, Danail Stoyanov, Diana Mateus, Maria A. Zuluaga, S. Kevin Zhou, Daniel Racoceanu, and Leo Joskowicz, editors, *Medical Image Computing and Computer Assisted Intervention – MICCAI 2020*, Lecture Notes in Computer Science, pages 710–719, Cham, 2020. Springer International Publishing. ISBN 978-3-030-59728-3. doi: 10.1007/978-3-030-59728-3_69.

Brian L. Trippe and Richard E. Turner. Conditional Density Estimation with Bayesian Normalising Flows, February 2018. URL http://arxiv.org/abs/1802.04908. arXiv:1802.04908 [stat].

Nicholas J. Tustison, Brian B. Avants, Philip A. Cook, Yuanjie Zheng, Alexander Egan, Paul A. Yushkevich, and James C. Gee. N4ITK: Improved N3 Bias Correction. *IEEE transactions on medical imaging*, 29(6):1310–1320, June 2010. ISSN 0278-0062. doi: 10.1109/TMI.2010.2046908. URL https://www.ncbi.nlm.nih.gov/pmc/articles/PMC3071855/.

Rama K. Vasudevan, Maxim Ziatdinov, Lukas Vlcek, and Sergei V. Kalinin. Off-the-shelf deep learning is not enough, and requires parsimony, Bayesianity, and causality. *npj Computational Materials*, 7(1):1–6, January 2021. ISSN 2057-3960. doi: 10.1038/s41524-020-00487-0. URL https://www.nature.com/articles/s41524-020-00487-0. Number: 1 Publisher: Nature Publishing Group.

Rongguang Wang, Pratik Chaudhari, and Christos Davatzikos. Harmonization with Flow-based Causal Inference, July 2021. URL http://arxiv.org/abs/2106.06845. arXiv:2106.06845 [cs, eess, stat].

Antoine Wehenkel and Gilles Louppe. You say Normalizing Flows I see Bayesian Networks, June 2020. URL http://arxiv.org/abs/2006.00866. arXiv:2006.00866 [cs, stat].

Antoine Wehenkel and Gilles Louppe. Graphical Normalizing Flows, February 2021. URL http://arxiv.org/abs/2006.02548. arXiv:2006.02548 [cs, stat].

Mengyue Yang, Furui Liu, Zhitang Chen, Xinwei Shen, Jianye Hao, and Jun Wang. CausalVAE: Disentangled Representation Learning via Neural Structural Causal Models. pages 9593–9602, 2021. URL https://openaccess.thecvf.com/content/CVPR2021/html/Yang_CausalVAE_Disentangled_Representation_Learning_via_Neural_Structural_Causal_Models_CVPR_2021_paper.html.

Jun-Yan Zhu, Taesung Park, Phillip Isola, and Alexei A. Efros. Unpaired Image-to-Image Translation Using Cycle-Consistent Adversarial Networks. In *2017 IEEE International Conference on Computer Vision (ICCV)*, pages 2242–2251, October 2017. doi: 10.1109/ICCV.2017.244. ISSN: 2380-7504.

Appendix A

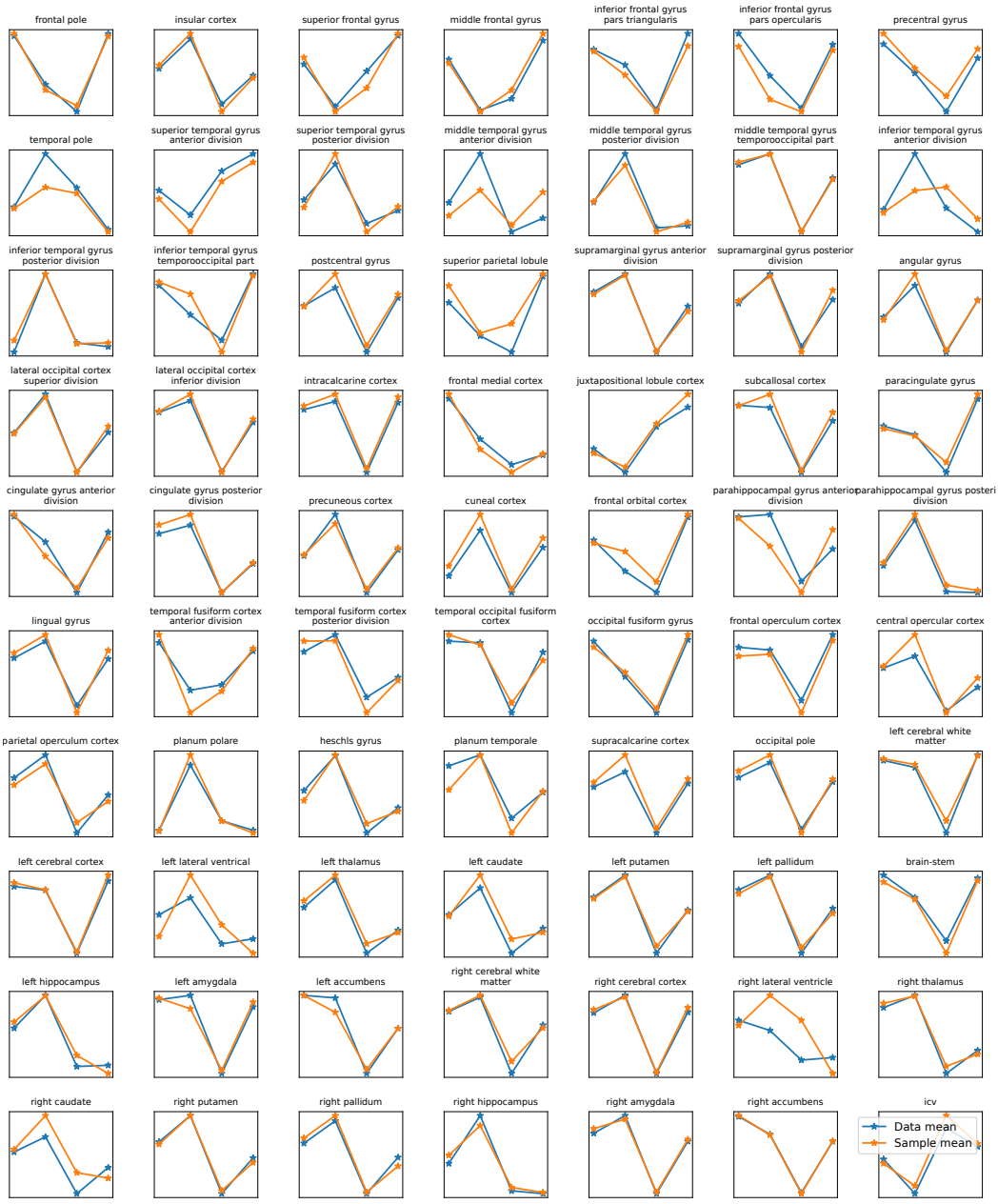

Figure 4: Blue: Mean values of the observational dataset features. Orange: the respective expected value of the learned probability density function using normalizing flows.

Appendix B

Table 2: Precision of classifiers trained with different base sites

Base site	Technique	C-BIG	JD	NC	Taowu	PMC	BC
-	-	0.76	0.56	0.52	0.71	0.59	0.28
C-BIG	CF	0.75	0.67	0.5	0.6	0.63	0.71
	ComBat	0.72	0.59	0.4	0.81	0.43	0.62
JD	CF	0.75	0.67	0.49	0.6	0.63	0.75
	ComBat	0.72	0.59	0.4	0.81	0.43	0.62
NC	CF	0.76	0.67	0.49	0.54	0.66	0.75
	ComBat	0.72	0.59	0.4	0.81	0.43	0.62
Taowu	CF	0.76	0.67	0.49	0.6	0.63	0.73
	ComBat	0.72	0.59	0.4	0.81	0.43	0.62
PMC	CF	0.76	0.67	0.49	0.6	0.6	0.71
	ComBat	0.72	0.59	0.4	0.81	0.43	0.62

Table 3: Recall of classifiers trained with different base sites

Base site	Technique	C-BIG	JD	NC	Taowu	PMC	BC
-	-	0.61	0.56	0.47	0.67	0.61	0.53
C-BIG	CF	0.58	0.61	0.53	0.6	0.65	0.68
	ComBat	0.61	0.61	0.59	0.67	0.51	0.55
JD	CF	0.58	0.61	0.53	0.6	0.65	0.74
	ComBat	0.61	0.61	0.59	0.67	0.51	0.55
NC	CF	0.61	0.61	0.53	0.53	0.67	0.71
	ComBat	0.61	0.61	0.59	0.67	0.51	0.55
Taowu	CF	0.61	0.61	0.53	0.6	0.65	0.71
	ComBat	0.61	0.61	0.59	0.67	0.51	0.55
PMC	CF	0.61	0.61	0.53	0.6	0.63	0.68
	ComBat	0.61	0.61	0.59	0.67	0.51	0.55